Multicomponent transport impact on turbulent premixed H_2/O_2 flames *

Julien de Charentenay† and Alexandre Ern‡§

† ONERA, F-92322 Châtillon, France and EM2C, ECP, F-92295 Châtenay-Malabry cedex, France

‡ CERMICS, Ecole nationale des ponts et chaussées, 6 et 8 avenue Blaise Pascal, F-77455 Marne la Vallée cedex 2, France

E-mail: ern@cermics.enpc.fr

Submitted to: *Combust. Theory Modelling*

Abstract. We investigate the impact of multicomponent transport on premixed turbulent H_2/O_2 flames. The present DNS database contains fifteen flame configurations where freely propagating planar flames interact with counterrotating vortices and synthetic turbulence fields. The DNS solver considers the conservation equations for species, momentum and energy with complex chemistry and detailed transport in two space dimensions and in the low Mach number regime. Accurate transport algorithms accounting for both multicomponent molecular and thermal diffusion are implemented in this solver at low computational costs. Multicomponent transport may lead locally in space or time to substantial modifications of turbulent flame properties. These modifications can be much larger than those observed for laminar flames. They are particularly noticeable on the propagation velocity and thus on the stretch in regions where the flame front experiences strong curvature effects. For most flames studied here, multicomponent transport has only a moderate impact on global flame properties because of the smoothing induced by turbulent fluctuations. Thus, the present DNS results, which for the first time incorporate detailed transport models, provide a form of a posteriori validation for previous DNS based on simplified transport models. However, for highly curved flames or when quenching phenomena arise, multicomponent transport plays a sufficiently relevant role to be included in accurate DNS.

* revised version (11 June 2002)

§ Corresponding author

1. Introduction

During the last decade, numerical investigations of turbulent flames using Direct Numerical Simulation (DNS) have provided very valuable information for the modeling of combustion processes. Recent examples include the ITNFS function [1] and countergradient diffusion phenomena [2]. Early simulations used a constant density approximation and considered a surface transport equation to represent turbulent flame propagation [3, 4]. More complex effects have been subsequently introduced, such as compressible equations in two [5] and three dimensions [6], while still retaining a one step chemistry model and a constant Lewis number approximation. DNS of multidimensional flames with complex chemistry have been reported recently, in both two [7–9] and three dimensions [10].

In the meantime, new results on multicomponent transport modeling for reactive flows have been obtained [11]. Based on a kinetic theory framework, it was shown that multicomponent transport coefficients could be expanded as convergent series [12, 13]. Detailed numerical investigations of combustion applications showed that accurate and cost effective approximations could be obtained by truncation, only retaining the first few terms in the convergent series [14]. In particular, these results paved the way to a thorough investigation of a particular multicomponent effect, known as the Soret effect, which results from species diffusion induced by temperature gradients. The Soret effect tends to drive light molecules towards hot regions of the flow and heavy molecules towards cold regions, thus affecting the flame structure. Numerical investigations on various laminar flame structures [15, 16] have shown that the Soret effect may have a significant impact locally on the flame structure for hydrogen flames but that this effect is less important for methane flames.

The goal of this work is to investigate the impact of multicomponent transport on turbulent premixed H_2/O_2 flames. Although we do not anticipate a dramatic impact of multicomponent transport on turbulent flame behavior, multicomponent transport phenomena may interact with turbulence and greatly modify turbulent flame properties at least locally in space or time. The question is then to determine whether these local perturbations are smoothed out by the turbulent fluctuations or may be amplified in space or time and have a global impact on the turbulent flame.

Our simulations will be based on hydrodynamic perturbations of freely propagating, planar, laminar flames. Perturbations will be generated by either a pair of counterrotating vortices or a synthetic turbulence field. Altogether, we shall investigate fifteen turbulent flame configurations. For most flames studied in this work, multicomponent transport effects will remain localized in time and in space. For such flames, our work will thus serve as an a posteriori validation for previous DNS based on simplified transport models. However, we will also point out some flame configurations where detailed transport models are needed for accurate DNS.

One important assumption made in this work is to restrict our simulations to two-dimensional flame structures. While this assumption alleviates considerably the burden

placed on computational resources and allows for a more systematic investigation of turbulent flame structures, it may be justified in part by previous three-dimensional DNS of turbulent premixed flames with single-step chemistry. Indeed, these simulations showed that the probability of finding cylindrical flame sheets is higher than that of finding spherical flame sheets [17]. It is thus reasonable to expect that the conclusions drawn from this study, at least as far as multicomponent transport is concerned, should remain valid for more realistic turbulent flames.

The paper is organized as follows. In the next section, we present the governing equations with complex chemistry and multicomponent transport used in the present DNS solver. In section 3, we briefly describe the planar flame database on which the DNS computations rely. In section 4, we detail the postprocessing tools used to extract both local and global flame properties. In sections 5 and 6, we investigate flame/vortex and flame/turbulence interaction and identify the impact of multicomponent transport.

2. Physical and Numerical Models

In this section, we present the conservation equations for multicomponent reactive flows in the low Mach number regime along with the physical models for chemical source terms and transport fluxes. We also detail the numerical methods used in the DNS solver.

2.1. Governing equations

The conservation equations for multicomponent reactive flows in fully compressible form are given in several classical textbooks [11, 18–21]. These equations express the conservation of species mass, momentum and energy and are completed by a state law equation. In this work, we shall assume an ideal mixture of perfect gases.

Many practical combustion applications involve low Mach number flows. In such cases, the compressible multicomponent equations often lead to numerical difficulties [22]. Indeed, the ratio of advective to acoustic time scales is very small, thus placing a severe limitation on the time step for explicit time integration schemes such as those used in DNS. This limitation may be circumvented by considering a low Mach number approximation based on an analysis of the order of magnitude of the various terms in the conservation equations [19,20,23]. In this approximation, the pressure is split into a thermodynamic, spatially uniform part p_0 and a hydrodynamic, fluctuating part $\widetilde{p}$ such that $\widetilde{p}/p_0$ is of the order of the square of the Mach number. The fluctuating pressure only arises in the momentum equations while the thermodynamic one is used in the state law. Furthermore, the viscous dissipation and the pressure work may be neglected in the energy conservation equation.

In turbulent flames, important couplings between pressure waves, flow patterns and chemical reactions may arise. Examples include self ignition phenomena in vortices [24], acoustic forcing on premixed flames [25] and closed vessel combustion [26]. However,

DNS of premixed turbulent H_2/O_2 flames such as those considered in this work has shown that the compressible and the low Mach number approaches yielded the same flame structures in open configurations [27]. Therefore, the present study relies on the low Mach number formulation and as far as the impact of multicomponent transport is concerned, its conclusions should directly carry over to the fully compressible formulation.

Letting t be the time and x the spatial coordinate vector, the governing equations read

$$\partial_t (\rho Y_k) + \partial_x \cdot (\rho v Y_k) + \partial_x \cdot F_k = \omega_k, \qquad k = 1, N_s, \tag{1}$$

$$\partial_t (\rho v) + \partial_x \cdot (\rho v \otimes v + \widetilde{p} I) + \partial_x \cdot S = 0, \tag{2}$$

$$\rho c_p \partial_t T + \rho c_p v \cdot \partial_x T + \partial_x \cdot Q = -\sum_{k=1}^{N_s} c_{p_k} F_k \cdot \partial_x T - \sum_{k=1}^{N_s} h_k \omega_k, \tag{3}$$

where ρ is the density, Y_k the mass fraction of the kth species, F_k its mass diffusion flux, ω_k its mass production rate, c_{p_k} its specific heat capacity at constant pressure, h_k its specific enthalpy, N_s the total number of species, v the hydrodynamic velocity, I the identity matrix, S the momentum flux tensor ($-S$ is the viscous stress tensor), $c_p = \sum_{k=1}^{N_s} Y_k c_{p_k}$ the mixture specific heat capacity at constant pressure, T the temperature and Q the thermal part of the heat flux vector. The governing equations (1)–(3) are completed by the state law

$$p_0 = \frac{\rho R T}{m}, \tag{4}$$

where R is the ideal gas constant, $m = (\sum_{k=1}^{N_s} Y_k / m_k)^{-1}$ the mean molecular mass of the mixture and m_k the molecular mass of the kth species.

The governing equations (1)–(3) are completed with boundary conditions. In the present work, we focus on two-dimensional turbulent flames resulting from perturbations of freely propagating flat laminar premixed flames. Periodic boundary conditions are imposed in the transverse direction, Dirichlet conditions at the inflow boundary and non-reflecting conditions at the outflow boundary.

2.2. Chemical source terms

We consider a chemical reaction mechanism for H_2/O_2 flames involving $N_s = 9$ species and $N_r = 19$ elementary reactions [28]. The reaction mechanism may be written in the form

$$\sum_{k=1}^{N_s} \nu_{ki}^f S_k \leftrightarrows \sum_{k=1}^{N_s} \nu_{ki}^b S_k, \qquad i = 1, N_r,$$

where N_r is the total number of reactions, ν_{ki}^f and ν_{ki}^b the forward and backward stoichiometric coefficients, and S_k the symbol of the kth species. The mass production

rates are then expressed as

$$\omega_k = m_k \sum_{i=1}^{N_r} \left(\nu_{ki}^b - \nu_{ki}^f\right) \left(K_{fi} \prod_{l=1}^{N_s} c_l^{\nu_{li}^f} - K_{bi} \prod_{l=1}^{N_s} c_l^{\nu_{li}^b}\right)$$

where K_{fi} and K_{bi} are the forward and backward rate constants of the ith reaction and c_l the molar concentration of the lth species. The forward rate constant is evaluated using an Arrhenius law while the reverse rate constant is given by the ratio of the forward rate constant divided by the equilibrium constant as given by thermodynamics. More details, including third body modifications, are given in [20].

2.3. Transport fluxes

The general expression of the transport fluxes S, Q and F_k is derived from the kinetic theory of gases [11, 20, 29]. The momentum flux tensor S reads

$$S = -\mu \left(\partial_x v + \partial_x v^t - \tfrac{2}{3} \left(\partial_x \cdot v\right) I\right), \tag{5}$$

where μ is the shear viscosity. The volume viscosity contribution is not included in (5) since it can be incorporated in the hydrodynamic pressure for low Mach number flows. On the other hand, the species mass diffusion fluxes and the thermal part of the heat flux vector read

$$F_k = -\sum_{l=1}^{N_s} \rho Y_k D_{kl} \left(\partial_x X_l + X_l \widetilde{\chi}_l \partial_x \log T\right), \tag{6}$$

$$Q = -\lambda \partial_x T + \frac{p_0}{\rho} \sum_{l=1}^{N_s} \frac{\widetilde{\chi}_l}{m_l} F_l, \tag{7}$$

where $D = (D_{kl})_{1 \le k,l \le N_s}$ is the multicomponent diffusion matrix, X_l the mole fraction of the lth species, $\widetilde{\chi} = (\widetilde{\chi}_l)_{1 \le l \le N_s}$ the rescaled thermal diffusion ratios and λ the thermal conductivity. The species diffusion fluxes result from two contributions: multicomponent molecular diffusion due to mole fraction gradients and the Soret effect due to temperature gradients. In the same way, the thermal part of the heat flux vector results from a classical Fourier contribution due to temperature gradients and a coupling term with the species diffusion fluxes known as the Dufour effect.

The kinetic theory of gases yields expressions for the transport coefficients μ, D, $\widetilde{\chi}$ and λ which involve the solution of constrained singular linear systems. The mathematical structure of these systems has been investigated in [11, 13]. In particular, it was shown that the transport coefficients could be expanded as convergent series. Fast and accurate approximate expressions were then obtained by truncation [12].

Optimized transport algorithms for flame codes have been investigated in [14]. Based on this work, we evaluate the shear viscosity by performing one conjugate gradient iteration on the usual transport linear system of size N_s [11]. The resulting expression is more accurate and less expensive to evaluate than the empirical Wilke approximation. On the other hand, the thermal conductivity and the rescaled thermal diffusion ratios

are evaluated from a linear system of size N_s based on the species total energy only [30]. The size of the linear system is thus half the size of the classical linear system usually considered in the literature. When the thermal conductivity alone needs to be evaluated, one conjugate gradient iteration is performed whereas three iterations are used when both the thermal conductivity and the rescaled thermal diffusion ratios are computed. Finally, the Stefan-Maxwell-Boltzmann equations are considered to evaluate the species mass diffusion fluxes from a transport linear system of size N_s. The multicomponent diffusion matrix may then be expressed as a convergent series. The first term, denoted by $D^{[0]}$, takes the form of a projected diagonal matrix. It simply corresponds to the classical Hirschfelder-Curtiss approximation with a mass correction velocity [31]. Truncating the series one term further yields a projected dense matrix, denoted by $D^{[1]}$, that accounts for cross diffusion effects. Both approximate diffusion matrices are specified in [15] where more details on the transport linear systems are also given.

In the DNS performed in this work, we compare two models for the mass diffusion fluxes and the thermal part of the heat flux vector.

- model M1: Soret, Dufour and cross diffusion effects are accounted for

$$F_k = -\sum_{l=1}^{N_s} \rho Y_k D_{kl}^{[1]} \left(\partial_x X_l + X_l \widetilde{\chi}_l \partial_x \log T\right), \qquad Q = -\lambda \partial_x T + \frac{p_0}{\rho} \sum_{l=1}^{N_s} \frac{\widetilde{\chi}_l}{m_l} F_l.$$

- model M2: Soret, Dufour and cross diffusion effects are neglected

$$F_k = -\sum_{l=1}^{N_s} \rho Y_k D_{kl}^{[0]} \partial_x X_l, \qquad Q = -\lambda \partial_x T.$$

Other intermediate models, such as accounting for Soret and Dufour effects while neglecting cross diffusion terms, are not considered in the present study for the sake of brevity.

2.4. Numerical methods and implementation

The numerical schemes implemented in our DNS code provide a high level of accuracy and low dissipation properties. Spatial derivatives are computed with sixth order centered finite difference schemes and time integration is performed with a fourth order Runge-Kutta formulation adapted to low Mach number flows. The momentum equations (2) are divided into a predictor and a corrector step. In the predictor step, we integrate the convective and viscous terms while neglecting the pressure gradient. Between the two steps, the hydrodynamic pressure is determined from a Poisson equation that ensures mass conservation at each Runge-Kutta substep and at the end of the global time step. The Poisson equation is solved using a Fast Fourier transform along the periodic direction with streamwise derivatives discretized using a fourth order finite difference scheme. The resulting system is solved using a pentadiagonal direct solver. Finally, the pressure gradient is updated in the corrector step. This procedure is classical for low Mach number simulations and is detailed for instance in [32, 33].

Some reactions of the H_2/O_2 chemical scheme are associated with short characteristic times. Therefore, a fully explicit integration scheme would require very small time steps. We thus employ a point implicit integration procedure of the chemical source terms. The time steps are thus limited by diffusive characteristic times which scale as the square of the mesh size. In the present DNS, diffusive characteristic times are typically five times larger than acoustic time scales, thus making the low Mach number formulation quite beneficial for CPU reduction, as already reported in [27, 33].

Thermodynamic properties and chemical source terms are evaluated using the Chemkin II package [34] with vector optimization [35]. On the other hand, multicomponent transport coefficients are evaluated using the EGlib package with vector optimization [36]. In this package, all the transport linear systems are considered in their naturally symmetric form which is computationally more efficient than the nonsymmetric versions considered in other packages [37]. In our implementation, the computation of thermodynamic properties and chemical source terms requires typically 18% of the overall CPU time. Multicomponent transport evaluation accounts for 8% of the overall CPU time when using model M2. When thermal diffusion coefficients are also computed, the relative contribution of multicomponent transport to the overall CPU time only goes up to 11%.

3. Preprocessing: the Planar Flame Database

In this section, we briefly describe the simulation code used to build the planar flame database. We then present the six test cases selected for DNS computations.

3.1. Physical and numerical modeling of planar flames

For freely propagating, one-dimensional, laminar flames, the dependent unknowns are the species mass fractions, the temperature and the constant mass flow rate. The governing equations are thus the species conservation equations (1) and the energy conservation equation (3) completed by the ideal gas law (4). The physical models for complex chemistry and multicomponent transport are those presented in sections 2.2 and 2.3. Inflow boundary conditions of flux type are considered for species and temperature while the well-known cold boundary difficulty is treated by introducing an ignition temperature. Simple Neumann boundary conditions for species and temperature are imposed at the outflow boundary. More details are given in [16].

The governing equations are discretized with second order finite difference schemes. The nonlinear set of discrete equations is solved approximately using damped Newton iterations. The thin regions of high chemical activity in the flame are appropriately resolved by adaptive gridding techniques. More details are given in [38, 39].

3.2. Test cases

In this work, we have selected six freely propagating, one-dimensional, laminar $H_2/O_2/N_2$ flame structures with equivalence ratios ϕ ranging from lean ($\phi = 0.5$) to rich ($\phi = 5$) and fresh gas temperatures T_u ranging from 300 K to 800 K. Table 1 presents the main characteristics of the six flame structures, referred to as test cases A to F. The burnt gas temperature T_b and the laminar flame speed S_l result from the one-dimensional simulations. Two flame lengths are evaluated, one based on the thermal thickness given by $\delta_l^T = (T_b - T_u)/|\partial_x T|_{max}$ and one based on the assumption of unity Reynolds number in the fresh gases, i.e. $\rho_u S_l \delta_l^{\mathrm{Re}}/\mu_u = 1$, where ρ_u and μ_u denote respectively the density and viscosity of the unburnt mixture. We may then define a laminar flame time as $t_F = \delta_l^T/S_l$.

In order to represent the flame structure, we introduce a progress variable c based on the temperature

$$c = \frac{T - T_u}{T_b - T_u}. \tag{8}$$

Since the temperature profile is monotone, the progress variable ranges from $c = 0$ in the fresh gases to $c = 1$ in the burnt gases. This property is not guaranteed when the progress variable is based on fuel or oxidizer mass fraction. Indeed, because of differential diffusion, these mass fractions may reach extremum values which differ from the unburnt or burnt values. We define the flame front by the isolevel $c = c^*$, where c^* corresponds to the value of the progress variable at the position of maximum heat release.

For each test case, two sets of values are reported in table 1, corresponding to models M1 and M2. Slight differences between predicted flame properties are observed. In particular, laminar flame speeds are lower with model M1 which accounts for thermal diffusion. Indeed, the Soret effect inhibits the diffusion of active chemical radicals such as H, O and OH from the hot to the cold regions around the flame front, thus making flame propagation slower. In the present test cases, laminar flame speeds predicted by model M1 are reduced by a factor ranging from 3% up to 7%, in quantitative agreement with the results reported in [16]. We also note that the maximum level of H mass fraction is slightly lower with model M1 (the most significant difference, observed for test case B, is 5%). Positive or negative variations of the same order of magnitude are observed for the H_2O_2 mass fraction. Finally, with the exception of test case C, slightly higher values are obtained for c^* with model M1.

One-dimensional laminar flame structures are converted into two-dimensional profiles by simple invariance in the y direction. The DNS meshes consist of square cells whose size is chosen adaptively for each test case by ensuring that at least ten cells are available in the x direction to resolve the sharp profiles of HO_2 and H_2O_2 radicals. The initial solution for the DNS calculations is then obtained by superimposing a velocity perturbation corresponding to either a pair of counterrotating vortices or a given synthetic turbulence field. Test cases A, B and C will be used to investigate

	ϕ	T_u (K)	T_b (K)	S_l (m/s)	δ_l^T (10^{-2}cm)	δ_l^{Re} (10^{-4}cm)	c^*
A^{M1}	0.5	300	1618	0.51	4.22	36.7	0.581
A^{M2}	0.5	300	1615	0.53	4.12	34.8	0.576
B^{M1}	1	300	2373	2.13	3.27	9.9	0.281
B^{M2}	1	300	2380	2.30	3.26	9.2	0.261
C^{M1}	5	300	1416	0.82	6.47	44.0	0.622
C^{M2}	5	300	1416	0.83	6.61	43.5	0.626
D^{M1}	0.5	800	2212	10.25	5.29	9.88	0.316
D^{M2}	0.5	800	2213	10.66	5.31	9.49	0.315
E^{M1}	1.0	800	2850	18.30	4.59	6.89	0.284
E^{M2}	1.0	800	2850	19.15	4.64	6.59	0.276
F^{M1}	1.3	800	2932	22.32	4.18	6.60	0.296
F^{M2}	1.3	800	2932	23.53	4.24	6.26	0.287

Table 1. Laminar flame parameters.

flame/vortex interaction whereas test cases A, D, E and F will be used to investigate flame/turbulence interaction.

4. Postprocessing Tools

In this section, we specify the local flame properties on which the impact of detailed transport models will be investigated. We also describe the numerical procedures used to access global flame properties in terms of standard and surface mean values from the DNS results.

4.1. Local flame properties

In this work, we represent turbulent flame structures using the progress variable c given by (8). Indeed, in our simulations, the turbulence field did not affect the maximum temperature so that the progress variable c always ranged from 0 to 1. The flame front is tracked by considering the isolevel $c = c^*$ with c^* determined from the planar flame database. The flame surface area S_f is then defined as the length of the isolevel $c = c^*$ in the computational domain. Note that our approach implicitly assumes that a flame always exists at the isolevel $c = c^*$ and that the local turbulent flame structure is sufficiently close to the laminar one. This assumption is reasonably valid in the flamelet

regime and will be further discussed below.

The conservation equation for the progress variable directly results from the energy conservation equation (3) and may be expressed as a Huygens (or G-) equation

$$\partial_t c + u \cdot \partial_x c = S_d \left| \partial_x c \right|, \tag{9}$$

with the propagation velocity S_d defined as

$$S_d = \frac{1}{\rho c_p \left| \partial_x T \right|} \left(-\partial_x \cdot Q - \sum_{k=1}^{N_s} c_{pk} F_k \cdot \partial_x T - \sum_{k=1}^{N_s} h_k \omega_k \right). \tag{10}$$

We can identify a direct impact of multicomponent transport on the propagation velocity through the species diffusion fluxes and the heat flux. Multicomponent transport has also an indirect influence on this velocity since it modifies the species profiles near flame fronts and thus impacts the heat release term. Our numerical results show that the indirect contribution is by far more important than the direct one.

Using simple geometrical considerations, the normal vector to the flame front may be defined as $n = -\partial_x c / \left| \partial_x c \right|$, the curvature radius of the flame front as $R_c = 1/\partial_x \cdot n$ and the tangential strain rate as $a_T = tt : \partial_x v$, where t is the tangential vector to the flame front. The local stretch rate K is defined as

$$K = a_T + \frac{S_d}{R_c}, \tag{11}$$

and its sign indicates local flame surface creation or consumption [40].

4.2. Global flame properties

Upon applying an ensemble averaged operator $\langle \cdot \rangle_S$ to the balance equation of flame surface area per unit volume [40, 41], an equation for the flame surface density Σ may be derived in the following form [6, 17]

$$\partial_t \Sigma + \partial_x \cdot \widetilde{v} \Sigma + \partial_x \cdot \langle v'' \rangle_S \Sigma + \partial_x \cdot \langle S_d n \rangle_S \Sigma = \langle \widetilde{a}_T \rangle_S \Sigma + \langle a_T'' \rangle_S \Sigma + \left\langle \frac{S_d}{R_c} \right\rangle_S \Sigma, \tag{12}$$

where $\widetilde{v}$ and v'' are respectively the Favre averaged and the fluctuating components of the velocity vector. In addition, we have $\langle a_T \rangle_S = \langle \widetilde{a}_T + a_T'' \rangle_S$ where $\langle \widetilde{a}_T \rangle_S = \langle tt \rangle_S : \partial_x \widetilde{v}$ and $\langle a_T'' \rangle_S = \langle tt : \partial_x v'' \rangle_S$ denote respectively the Favre averaged and the fluctuating components of the tangential strain rate. Equation (12) contains time evolution and advective terms on the left side and production/consumption terms on the right side. The right member may be directly expressed in terms of the ensemble averaged value of the stretch.

In order to postprocess our DNS results, we introduce discrete standard and surface mean operators. We consider a structured mesh composed of rectangular cells. We denote by N_x (resp. N_y) the number of cells in the x (resp. y) direction and by dx (resp. dy) the cell size. For the sake of simplicity, we assume a constant mesh size in both x and y directions although the procedures described hereafter easily extend to nonuniform meshes. We denote by C_{ij} the cell whose lower left vertex has indices i and j.

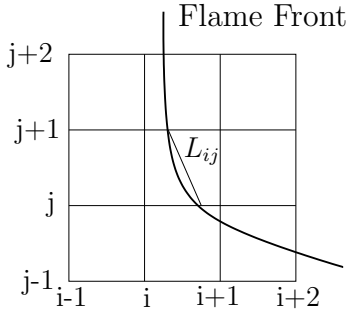

Figure 1. Definition of local flame length L_{ij} in cell C_{ij}.

We first define the standard mean operator $\langle\cdot\rangle$ as the standard mean value along the periodic direction y. This operator is defined for cell centered variables. Let Q be one of such variables and let Q_{ij} denote its constant value in cell C_{ij}. The standard mean operator reads

$$\langle Q\rangle(i) = \frac{1}{N_y}\sum_{j=1}^{N_y} Q_{ij},$$

and is thus a function of the streamwise coordinate i. Let now $\mathcal{A}$ be the cell averaging operator which maps a nodal variable x into a cell centered variable $\mathcal{A}x$ defined as $(\mathcal{A}x)_{ij} = (x_{ij} + x_{i+1\,j} + x_{i\,j+1} + x_{i+1\,j+1})/4$. With this operator, the standard mean operator can also be applied to nodal variables x simply by evaluating $\langle\mathcal{A}x\rangle$. For instance, the Favre averaged value of the progress variable reads

$$\widetilde{c} = \langle\mathcal{A}(\rho c)\rangle \,/\, \langle\mathcal{A}\rho\rangle\,.$$

In order to evaluate a discrete flame surface density, we introduce the length L_{ij} of the isolevel $c = c^*$ in cell C_{ij} (figure 1). The flame surface density, still denoted by Σ, then reads

$$\Sigma(i) = \frac{1}{dx\,dy}\frac{1}{N_y}\sum_{j=1}^{N_y} L_{ij},$$

and its unit is thus the reciprocal of a length. With this definition, the flame surface density is a cell centered quantity defined along the streamwise direction. It differs from the previous definition of [6] where components of the normal vector at constant x values were considered.

Finally, similarly to [6], we introduce a flame surface mean operator $\langle\cdot\rangle_S$ for nodal variables. Let f be one of such variables and denote by f_{ij} its value at the midpoint of segment L_{ij}. The flame surface mean operator then reads

$$\langle f\rangle_S(i) = \frac{\sum_{j=1}^{N_y} f_{ij}L_{ij}}{\sum_{j=1}^{N_y} L_{ij}}, \tag{13}$$

and is defined for all indices i such that $\sum_{j=1}^{N_y} L_{ij} \neq 0$.

5. Flame/Vortex Interaction

The DNS database for flame/vortex interaction contains eight test cases based on laminar premixed flames A, B and C. The initial perturbation to the velocity field is given by a pair of counterrotating vortices as illustrated in figure 2.

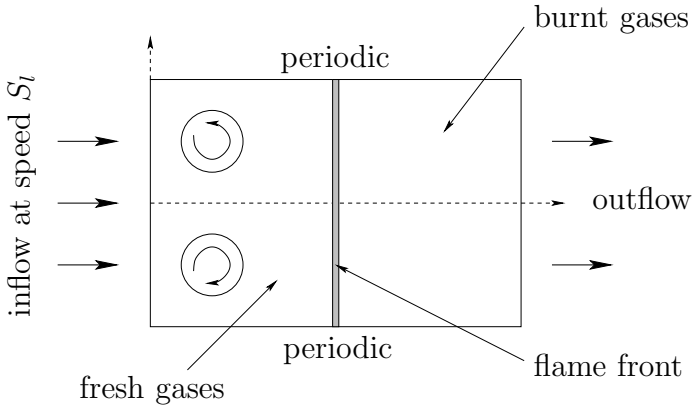

Figure 2. Initial configuration for flame/vortex interaction.

The vorticity of a single vortex is $\Gamma = \Gamma_0 \exp(-r^2/2r_V^2)$, where Γ_0 is the initial circulation, r_V the vortex radius and r the distance to the vortex center. The maximum vortex induced velocity is given by $u'_V = (\Gamma_0/r_V)e^{-1/2}$. The vortex centers are located at the distance of $1.5r_V$ from the symmetry axis and we denote by $R_V = 5r_V$ the vortex pair radius. With these parameters, we may define a vortex turnover time as $t_V = R_V/u'_V$. The vortex parameters u'_V and R_V are given in table 2. We also report the quantities N_x and L_x (resp. N_y and L_y) which denote the number of cells and the length of the computational domain in the x (resp. y) direction.

Case	u'_V (m/s)	R_V (mm)	t_V (ms)	$N_x \times N_y$	$L_x \times L_y$ (mm×mm)
AV1	10	2.10	0.21	500×250	10.0×5.0
AV2	10	0.67	0.067	500×100	10.0×2.0
AV3	5	2.10	0.42	500×250	10.0×5.0
BV1	44	1.63	0.037	900×512	7.0×4.0
BV2	44	0.52	0.012	900×192	7.0×1.5
CV1	16.4	3.25	0.20	500×326	10.0×6.5
CV2	16.4	1.04	0.06	500×100	10.0×2.0
CV3	8.2	3.25	0.40	500×326	10.0×6.5

Table 2. Vortex parameters for flame/vortex interaction.

The vortex parameters u'_V and R_V are chosen so that they yield three sets of flame/vortex length and velocity ratios: test cases V1 correspond to strong intensity and large radius vortices ($u'_V/S_l \sim 20$, $R_V/\delta_l^T \sim 5$), cases V2 to strong intensity and small radius vortices ($u'_V/S_l \sim 20$, $R_V/\delta_l^T \sim 1.6$), and cases V3 to weak intensity and large radius vortices ($u'_V/S_l \sim 10$, $R_V/\delta_l^T \sim 5$). Since the vortex parameters are identical for models M1 and M2, the flame/vortex length and velocity ratios slightly depend on the transport models through the laminar flame properties δ_l^T and S_l. In all cases, the vortex parameters are such that the flow Mach number is always smaller than $M \leq 0.1$, in agreement with the low Mach number approximation.

Various important flame behaviors are represented in this DNS database, including formation of fresh gas pockets, vortex dissipation by strongly curved flames and flame quenching. We refer to [5, 42–44] for a physical discussion of these phenomena.

5.1. Time evolution of turbulent flame structures

We display in figure 3 the time evolution of H_r defined as the heat release integrated over the computational domain. For cases AV1 to BV2, H_r increases sharply once the vortices have reached the flame front. A quite different behavior is observed for cases CV1 to CV3 since H_r first decreases with time, thus indicating flame quenching. Indeed, because of their high equivalence ratio, these flames are highly sensitive to velocity perturbations. For test case CV2, involving small vortices, flame reignition occurs at approximatively $t = 10t_V$ and yields to a sharp increase of H_r after $t = 12t_V$. Because of these quenching/ignition phenomena, we can consider that cases CV1 to CV3 are not located in the flamelet regime. Furthermore, we observe that the flame surface increases with time while the flame is being quenched, indicating that the isolevel $c = c^*$ is not appropriate to define the flame front. Similar considerations have been previously mentionned in [42, 44], but mainly for nonpremixed flames. Multicomponent transport has a significant influence on the time evolution of the heat release especially when quenching phenomena are present with relative variations of the order of 15%. In the other cases, its impact is mainly limited to the peak value reached by H_r with relative variations of the order of 5%.

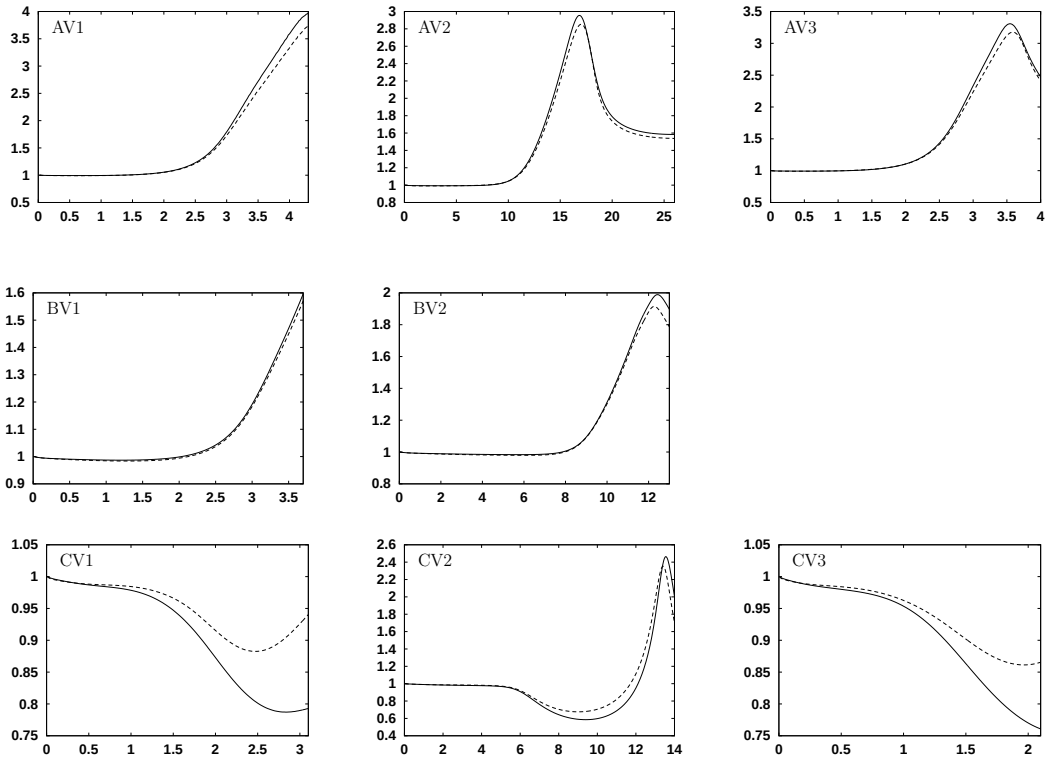

Figure 3. Time evolution of integrated heat release H_r obtained with models M1 (solid line) and M2 (dashed line). Time is normalized by the vortex turnover time t_V and H_r by its initial value.

Figure 4 presents the time evolution of the flame stretch K^* evaluated at the first point on the symmetry axis where $c = c^*$. In flame/vortex interaction, the strain rate contribution to the stretch is always positive while the curvature one is negative, so that the sign of the stretch depends on the relative size of both contributions. For large radius vortices (cases V1 and V3), the stretch is dominated by the strain rate and is thus positive. In cases AV1, BV1 and AV3, the vortex pair crosses the flame front without quenching it and leads to the formation of a fresh gas pocket surrounded by a flame. On the other hand, for small radius vortices (cases V2), a competition between strain and curvature arises and flame behavior depends on the equivalence ratio. For lean flames (case AV2), K^* immediately becomes negative, indicating that the vortices are dissipated by the strongly curved flame. For stoichiometric flames (case BV2), K^* first increases and then decreases at approximately $t = 11t_V$ showing that the vortices eventually manage to cross the flame front. Multicomponent transport impact on the time evolution of K^* remains marginal except for highly curved flames and especially for case BV2 where the relative variations are larger than 50% at approximately $t = 11t_V$.

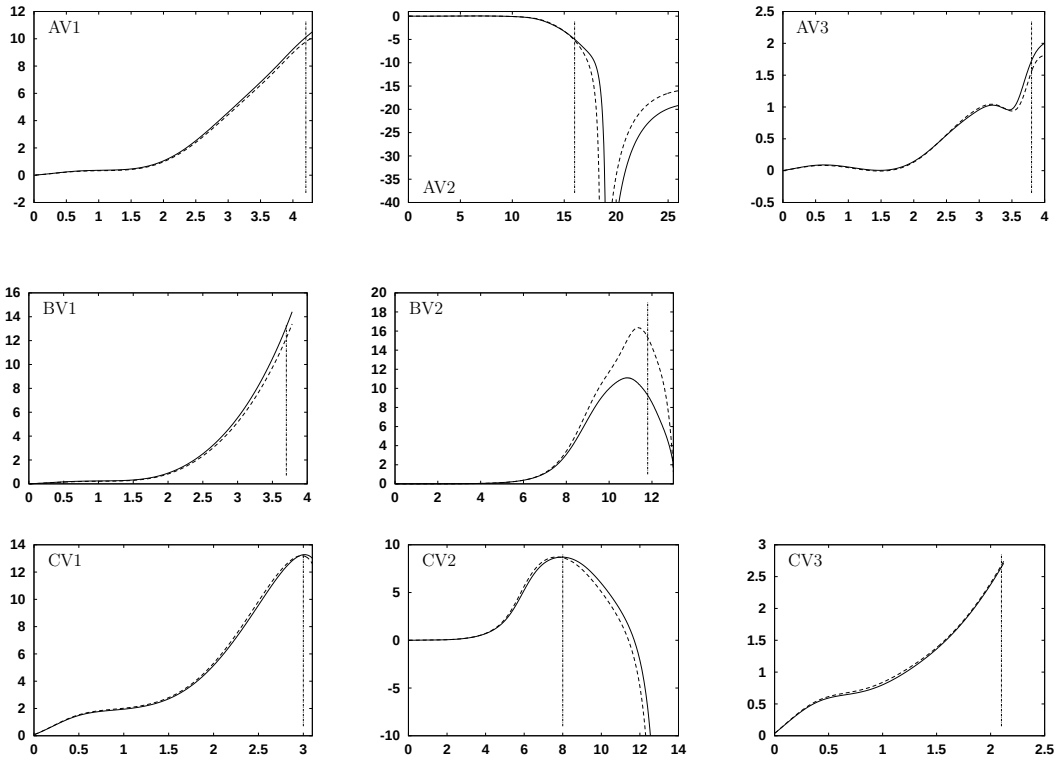

Figure 4. Time evolution of flame stretch K^* evaluated at the first point on the symmetry axis where $c = c^*$. Models M1 (solid line) and M2 (dashed line). Time is normalized by the vortex turnover time t_V and K^* by the laminar flame time t_F. Vertical lines indicate the times selected in section 5.2 to investigate instantaneous profiles.

5.2. Investigation of instantaneous profiles

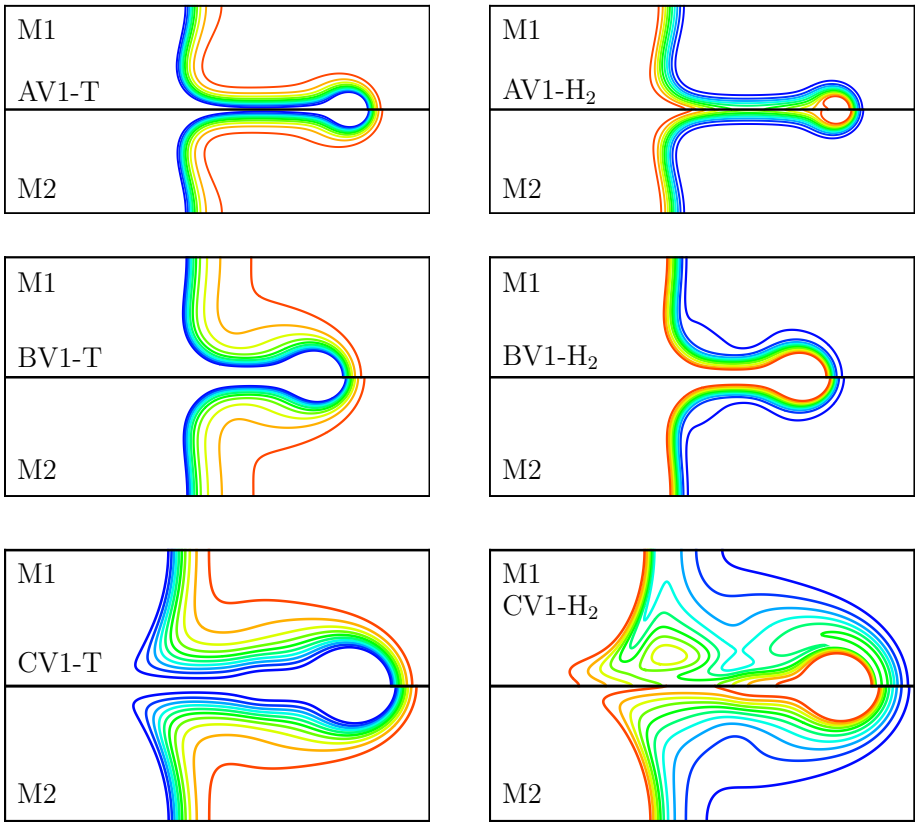

Figure 5. Isocontours for temperature and H_2 mass fraction. Cases AV1, BV1 and CV1 with models M1 and M2.

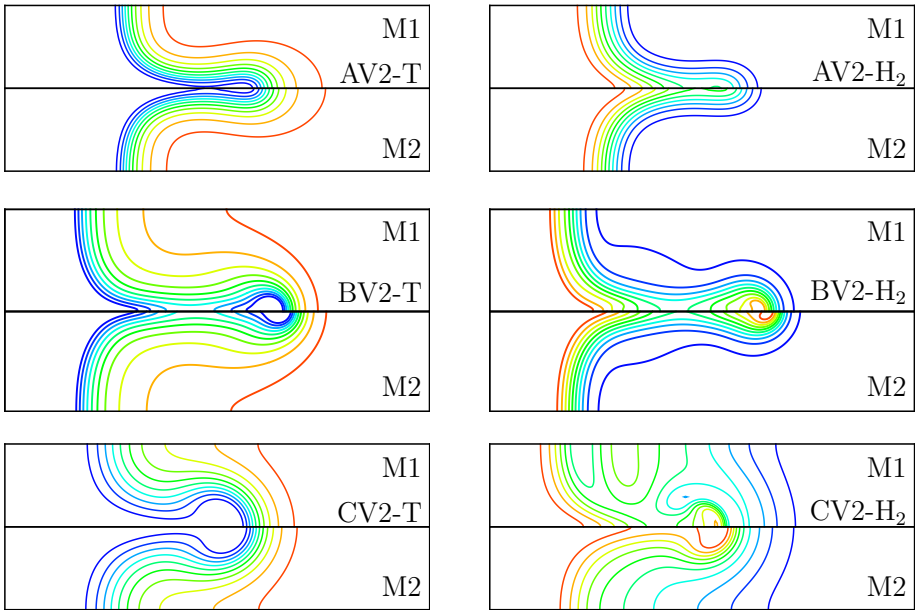

Figure 6. Isocontours for temperature and H_2 mass fraction. Cases AV2, BV2 and CV2 with models M1 and M2.

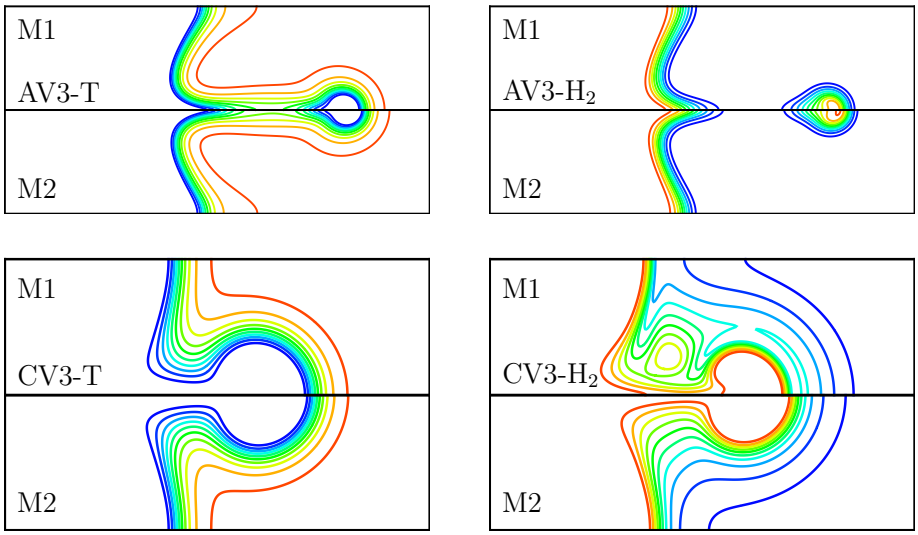

Figure 7. Isocontours for temperature and H_2 mass fraction. Cases AV3 and CV3 with models M1 and M2.

Figures 5, 6 and 7 present temperature and H_2 mass fraction isocontours for all test cases at the times selected in figure 4. The formation of the fresh gas pocket is clearly visible for cases AV1, AV3, BV1 and BV2. The pocket is still connected to the fresh gases in cases AV1 and BV1 whereas it is already separated in cases AV3 and BV2. We also observe the vortex dissipation by the strongly curved flame in case AV2. For cases CV1

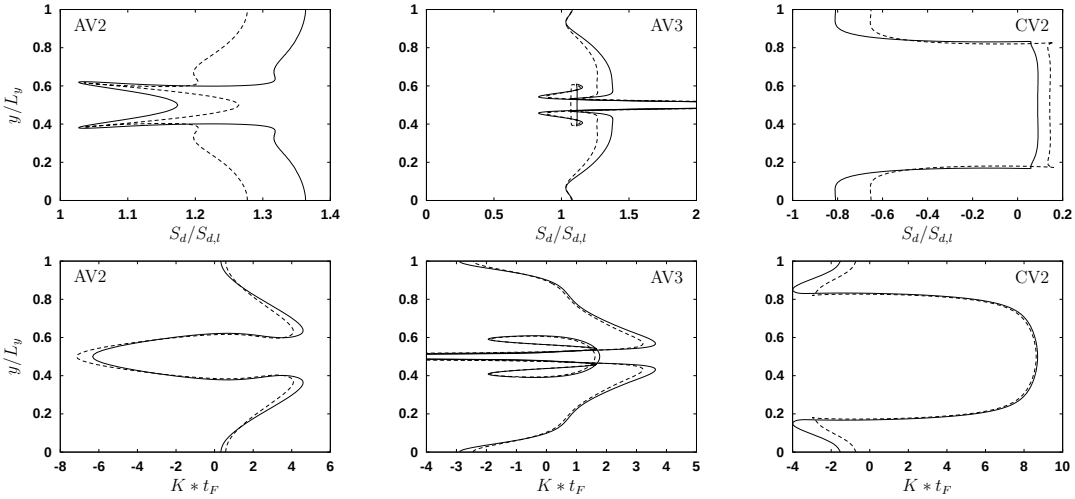

Figure 8. Propagation velocity S_d and flame stretch K extracted along the flame front as a function of the y coordinate. Cases AV2, AV3 and CV2 with models M1 (solid line) and M2 (dashed line). S_d is normalized by its laminar value $S_{d,l} = \rho_u S_l/\rho_{c^*}$, K by the laminar flame time t_F and y by L_y.

to CV3, the quenching phenomenon is more difficult to identify on the temperature or H_2 mass fraction. However, the impact of multicomponent transport on instantaneous profiles is quite significant on these cases. For example, in case CV3, the H_2 gas pocket is still linked to the fresh gas flow with model M2 while it is detached with model M1. Local differences are also present in the other cases especially at the leading and trailing edge of the fresh gas pocket.

Figure 8 presents the propagation velocity S_d and the flame stretch K extracted along the flame front as a function of the y coordinate for test cases AV2, AV3 and CV2 at the same times as those selected previously. For case AV2, which is representative of vortex dissipation, the stretch, which is dominated by curvature effects, is negative at the symmetry axis and relaxes back to zero at the periodic boundaries because of the small vortex radius. Multicomponent transport has a significant impact on the propagation velocity and thus also indirectly on the stretch. Model M1 yields lower propagation velocities around the symmetry axis, which can be attributed to the Soret effect. However, the impact near the periodic boundaries is opposite. For case AV3, which is representative of detached fresh gas pocket, we can identify two flame cusps at the leading edge of the main flame and at the trailing edge of the detached pocket. These cusps lead to almost singular behavior for flame stretch through velocity and curvature. In addition, the stretch takes large negative values at the periodic boundaries because of important flame bending. Model M1 leads to larger propagation velocities, especially at the leading edge of the detached pocket, in agreement with the observations of figure 7. Finally, for case CV2, which is representative of flame quenching, the propagation velocity is much smaller than its laminar value and even takes negative values near the periodic boundaries, indicating propagation towards the burnt gases. The impact of

multicomponent transport is quite significant, as already observed from figure 6. Model M1 mainly yields lower propagation velocities, which can be attributed to the Soret effect.

6. Flame/Turbulence Interaction

The DNS database for flame/turbulence interaction contains seven test cases based on laminar flames A, D, E and F. The initial perturbation to the velocity field is generated from either the Passot-Pouquet (PP) or the Von Kármán-Pao (VKP) turbulence spectrum. Both spectra are characterized by two parameters, the root mean square (r.m.s.) of the fluctuating velocity u' and the integral length scale Λ. With these two parameters, we may define a turbulence time $t_T = \Lambda/u'$. More details on the PP and VKP spectra are given in [45].

Table 3 presents the turbulence spectra with the corresponding parameter values for the seven test cases, as well as the number of cells $N = N_x = N_y$ and the length $L = L_x = L_y$ of the square computational domain. Table 3 also includes estimates for the Damköhler and Karlovitz numbers based on the expressions $\mathrm{Da} = (\Lambda/\delta_l^{\mathrm{Re}})(S_l/u')$ and $\mathrm{Ka} = (u'/S_l)^{3/2}(\Lambda/\delta_l^{\mathrm{Re}})^{-1/2}$. Test cases AT1 and AT2 correspond to a large velocity ratio u'/S_l and are located in the extended flamelet regime. The other test cases are in the standard flamelet regime based on the Klimov-Williams criterion $\mathrm{Ka} \leq 1$. In all cases, velocity fluctuations are such that $M \leq 0.2$, in agreement with the low Mach number approximation.

Case	Spectrum	u' (m/s)	Λ (cm)	N	L (cm)	Da	Ka
AT1	PP	5	0.1	500	1	3.0	5.59
AT2	VKP	4	0.1	500	1	3.7	4.00
DT1	PP	10	0.1	500	1.5	104.2	0.10
DT2	PP	10	0.3	500	1.5	312.5	0.06
ET1	PP	20	0.3	500	1.5	407.1	0.06
ET2	PP	30	0.3	500	1.5	279.9	0.10
FT1	PP	30	0.3	600	1.5	360.5	0.07

Table 3. Turbulent field parameters for flame/turbulence interaction.

6.1. Time evolution of turbulent flame structures

Flame wrinkling and chemical activity are estimated by the flame surface area, S_f, and the heat release integrated over the computational domain, H_r. Flame surface areas

are reported in figure 9 for all test cases while integrated heat releases are presented in figure 10 for two selected cases. The time evolution of flame surface area results from a competition between turbulent flame wrinkling and flame surface consumption when two flame elements merge together. All the flames remain statistically planar since the flame surface mean value of their curvature is nearly zero at all times. Two phenomena are observed for all test cases: (i) a sharp increase in flame surface area and integrated heat release over an establishment time and (ii) a strong correlation between these two quantities. In cases D, E and F, we also notice strong oscillations of the flame surface area resulting from the competition between turbulent wrinkling and flame surface consumption. In these cases, the flame front returns to its laminar state at the end of the simulation. Indeed, since we do not sustain the turbulence in the computational domain or through the boundary conditions, the turbulent perturbation is eventually convected through the flame out of the computational domain.

We observe some impact of multicomponent transport on flame wrinkling and chemical activity. In agreement with the previous analysis of flame/vortex interaction, multicomponent transport yields in most cases lower flame propagation velocities. Therefore, the flame surface consumption mechanism is less effective and also slightly delayed in time when detailed transport models are used. For instance, model M1 leads to a 7% higher maximum value of the flame surface area in case AT1. On the same token, the maximum increase of the normalized integrated heat release is underpredicted by 6% when using model M2. Note that the integrated heat release is normalized by its initial value which is different for models M1 and M2. The absolute maximum value of the integrated heat release with model M2 is 2% lower than with model M1 in case AT1 and 2% higher in case ET1.

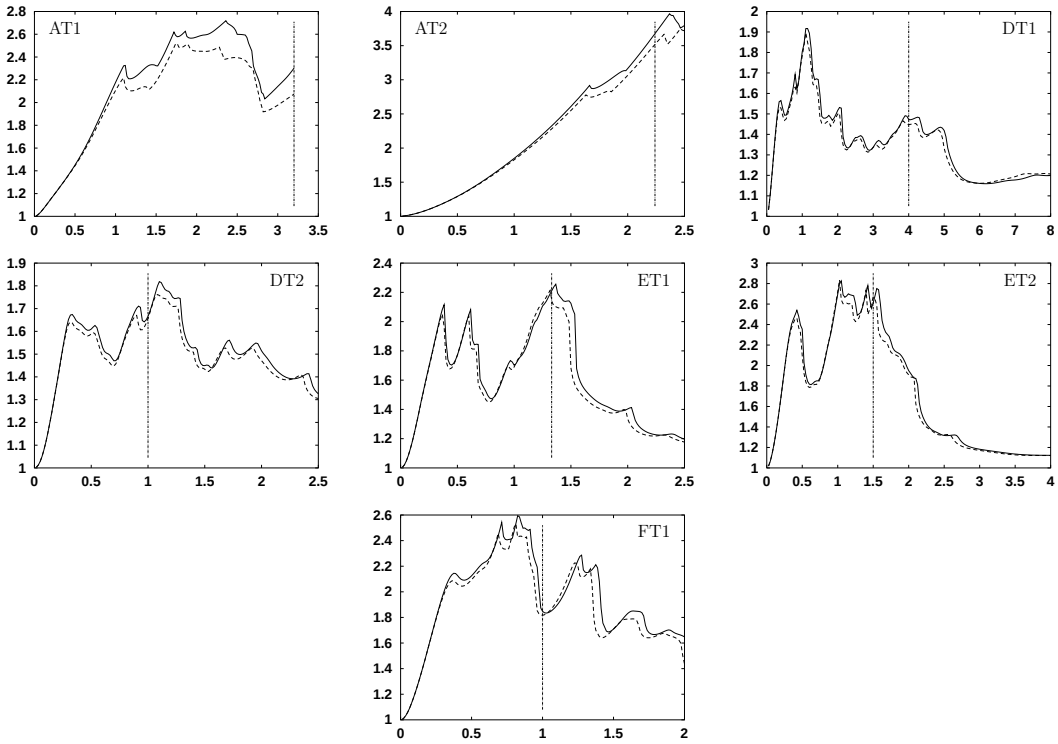

Figure 9. Time evolution of flame surface area S_f obtained with models M1 (solid line) and M2 (dashed line). Time is normalized by the turbulent time t_T and S_f by its initial value. Vertical lines indicate the times selected in section 6.2 to investigate instantaneous profiles.

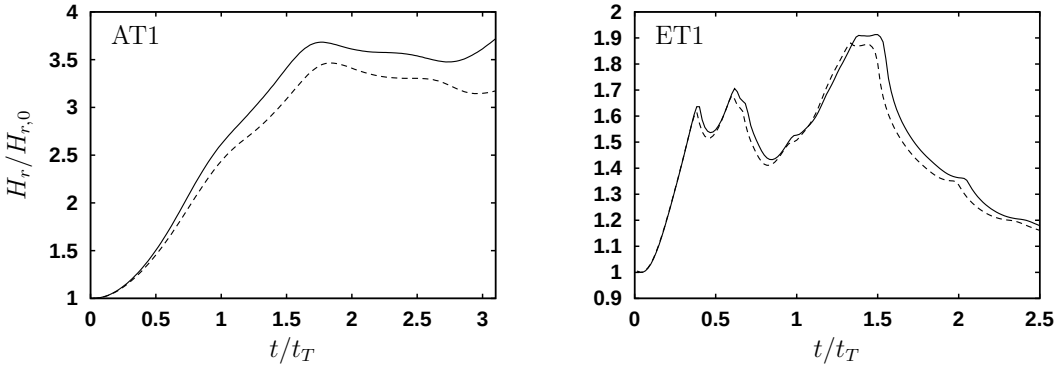

Figure 10. Time evolution of integrated heat release H_r obtained with models M1 (solid line) and M2 (dashed line). Cases AT1 and ET1. Time is normalized by the turbulent time t_T and H_r by its initial value $H_{r,0}$.

Figure 11 displays, for test cases AT1 and ET1, the time evolution of the flame surface mean value of the propagation velocity S_d given by (10). We report results obtained with models M1 and M2 as well as the r.m.s. of $\langle S_d \rangle_S$ obtained with model M1. For case AT1, $\langle S_d \rangle_S$ decreases at the very beginning of the simulation until approximately $t = 0.3t_T$ and then increases until it becomes larger than its laminar

value at approximately $t = t_T$. For case ET1, we obtain a different impact of the turbulence field since the turbulent flame velocity is most of the time lower than the laminar one. For both cases, we observe strong peaks that are local in time and correlate with consumption of flame surface area. Indeed, these peaks are related to the destruction of fresh gas pockets involving very high flame propagation velocities, thus strongly affecting the mean value $\langle S_d \rangle_S$. On the other hand, our results show that multicomponent transport has no sizeable overall impact on the flame surface mean value of flame properties such as propagation velocity as well as tangential strain rate or curvature. However, significant, local in time effects are observed at the peaks previously described. For case ET1, such effects may be of the same order of magnitude as the r.m.s. of turbulent fluctuations, but are much smaller for case AT1.

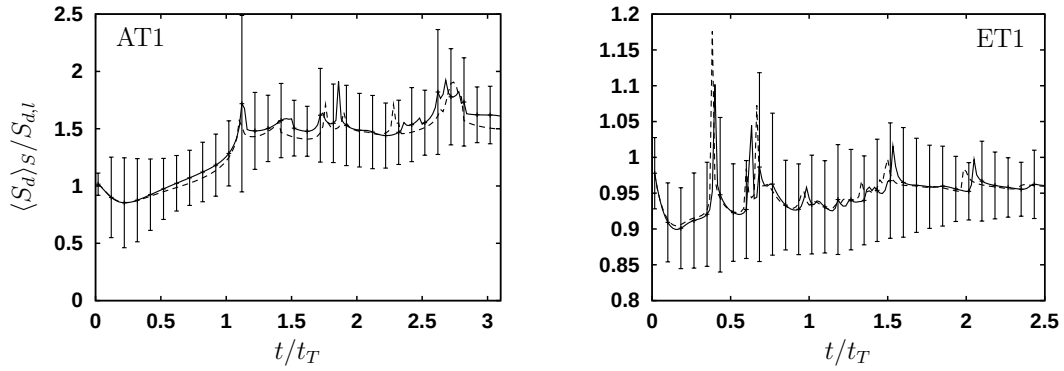

Figure 11. Time evolution of the flame surface mean value of propagation velocity $\langle S_d \rangle_S$ obtained with models M1 (solid line) and M2 (dashed line) and its r.m.s. obtained with model M1. Cases AT1 and ET1. Time is normalized by the turbulent time t_T and $\langle S_d \rangle_S$ by its laminar value $S_{d,l} = \rho_u S_l / \rho_{c^*}$.

6.2. Investigation of instantaneous profiles

Both local and statistical properties are investigated using an instantaneous field selected at the times indicated by a vertical line in figure 9. Figure 12 presents temperature and H mass fraction isocontours for cases AT1 and ET1 and for models M1 and M2. Isocontours obtained with models M1 and M2 are similar but not identical, with differences mainly arising in highly curved regions. In particular, when using model M1, the flame front movement is delayed and the flame surface is more wrinkled. The analysis of the other test cases leads to the same conclusions. These results are also in agreement with the time evolution of the flame surface area discussed previously.

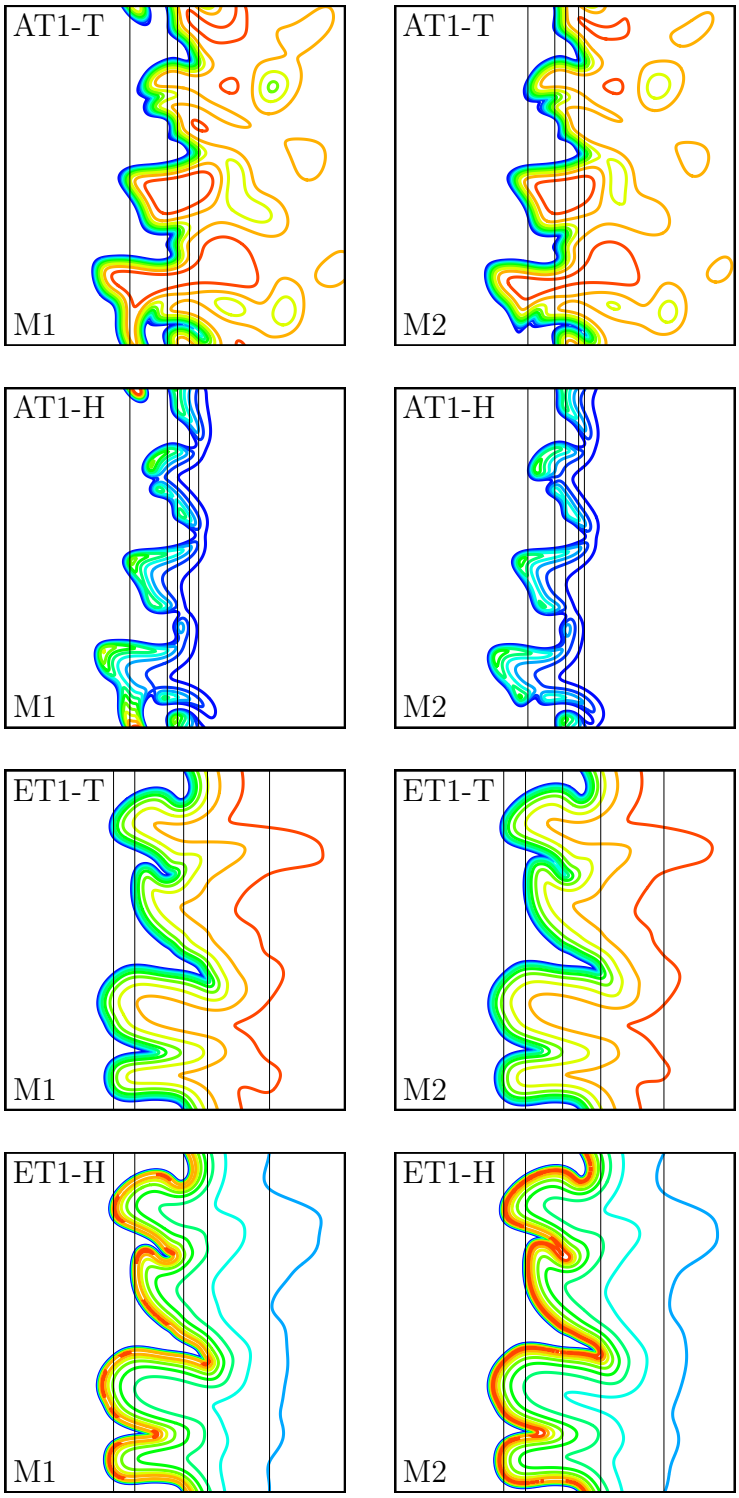

Figure 12. Isocontours for temperature and H mass fraction. Cases AT1 at time $t = 3.2t_T$ and ET1 at time $t = 1.33t_T$ with models M1 and M2. Vertical lines represent the position of the Favre averaged progress variable $\widetilde{c}$ for the values $\{0.1, 0.25, 0.5, 0.75, 0.9\}$.

For case AT1, which is located in the extended flamelet regime, front discontinuities appear in the H and O profiles with maximum H levels located in regions corresponding to positive curvature. However, such discontinuities do not appear in the H_2O_2 profile. Thus, various status of the flame can be inferred locally depending on the chemical radical that is considered to track the flame front, making the interpretation of the numerical results more complex for multicomponent DNS. In the following, we shall assume that the definition of the flame front given in section 4 remains valid also for cases AT1 and AT2.

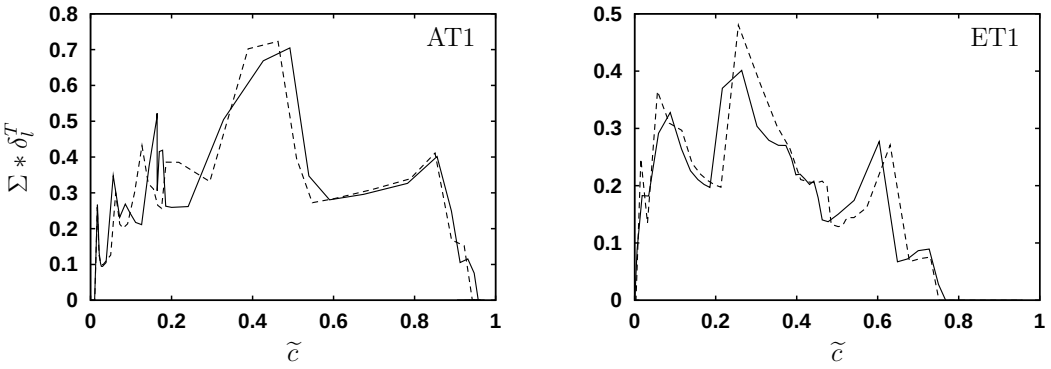

Figure 13. Flame surface density Σ normalized by the thermal flame thickness δ_l^T as a function of the Favre averaged progress variable $\widetilde{c}$. Cases AT1 and ET1 with models M1 (solid line) and M2 (dashed line).

Case	δ_{fb}^{M1}	$\frac{\delta_{fb}^{M2}-\delta_{fb}^{M1}}{\delta_{fb}^{M1}}$	σ_y^{M1}	$\frac{\sigma_y^{M2}-\sigma_y^{M1}}{\sigma_y^{M1}}$
AT1	0.322	- 7.5 %	0.645	7.5 %
AT2	0.690	- 3.8 %	0.717	0.0 %
DT1	0.243	- 1.2 %	0.569	- 0.4 %
DT2	0.363	2.5 %	0.470	- 2.1 %
ET1	0.468	1.3 %	0.719	- 0.6 %
ET2	0.648	3.2 %	0.671	- 0.4 %
FT1	0.490	0.0 %	0.560	0.4 %

Table 4. Mean values of the flame brush δ_{fb} (in cm) and of the orientation factor σ_y obtained with model M1 and relative error of model M2.

Figure 13, which presents the flame surface density Σ as a function of the Favre averaged progress variable $\widetilde{c}$, illustrates the spreading of the turbulent flame in the $\widetilde{c}$ space. Multicomponent transport does not impact the global shape of the Σ profile but may have a significant influence on local values. On the other hand, the flame

spreading in the physical space may be evaluated by considering the flame brush δ_{fb} which is defined as the length in the x direction for which the flame surface density is nonzero. This quantity is reported in table 4. The flame brush ranges from 24% of the computational domain for weak turbulence fields (case DT1) up to 69% for strong turbulence fields (case AT2). The impact of multicomponent transport on this quantity reaches 7.5% in case AT1. The flame brush is higher with model M1 for cases AT1 and AT2 for which the turbulent velocity is high compared to the laminar flame velocity. Table 4 also reports the orientation factor σ_y defined as in [6]. The mean values of the orientation factor range between $\sigma_y = 0.470$ and $\sigma_y = 0.719$. In most cases, this value is higher than the one proposed by Bray [46], $\sigma_y = 0.5$. The impact of multicomponent transport on this quantity is marginal except for case AT1 where it reaches 7.5%.

Figure 14 displays the flame surface mean value of the propagation velocity $\langle S_d \rangle_S$ as a function of Favre averaged progress variable $\widetilde{c}$ for cases AT1 and ET1. In case AT1, $\langle S_d \rangle_S$ is greater than its laminar value and also decreases with $\widetilde{c}$ up to $\widetilde{c} = 0.7$. This behavior indicates that the flame brush is locally increasing in time since the flame front is propagating faster in the fresh gas region than in the flame core. This effect is slightly enhanced when model M1 is considered. Similar results have been observed in [6] for constant Lewis simulations when the Lewis number was decreased from 0.8 to 0.3, keeping in mind that the inclusion of the Soret effect in model M1 may be interpreted as a decrease in the overall Lewis number for hydrogen. On the other hand, for case ET1, $\langle S_d \rangle_S$ is lower than its laminar value but no specific behavior is observed in the fresh gases. Finally, we observe in all cases and for both multicomponent transport models that the broadening of the turbulent flame is limited by the propagation velocity at its trailing edge which is larger than in the turbulent flame core.

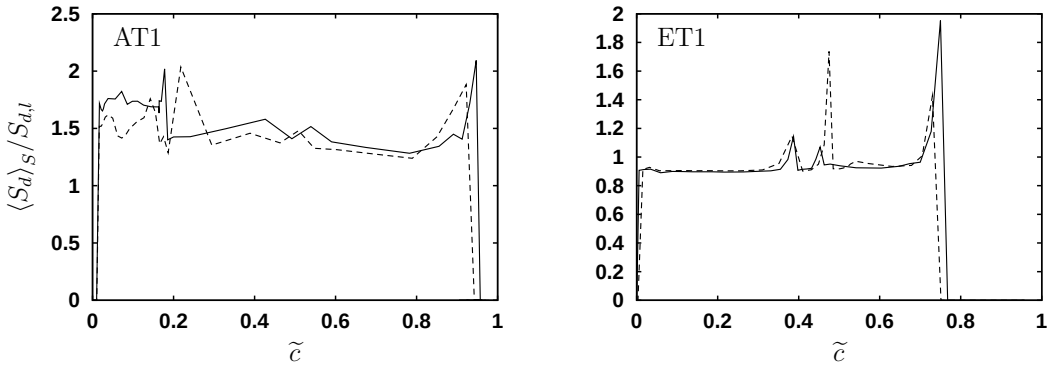

Figure 14. Flame surface mean value of the propagation velocity $\langle S_d \rangle_S$ normalized by its laminar value $S_{d,l}$ as a function of the Favre averaged progress variable $\widetilde{c}$. Cases AT1 and ET1 with models M1 (solid line) and M2 (dashed line).

Figure 15 deals with the various source terms in the flame surface density equation (12). Our results are in agreement with previous DNS results [6]. In particular, the mean flow induced strain rate is not negligible with respect to the total strain rate and both contributions are mainly positive. For most cases, multicomponent transport

has a significant effect locally in the $\widetilde{c}$ space. For example, in case AT1, the effect is particularly important in the fresh gases, but in other test cases, the effect was observed in different regions of the turbulent flames. Also in agreement with [6], the propagation term $\langle S_d/R_c \rangle_S$ is positive in the fresh gases and negative in the burnt gases. The impact of multicomponent transport is again local and qualitatively similar to the one discussed for the propagation velocity alone in figure 14.

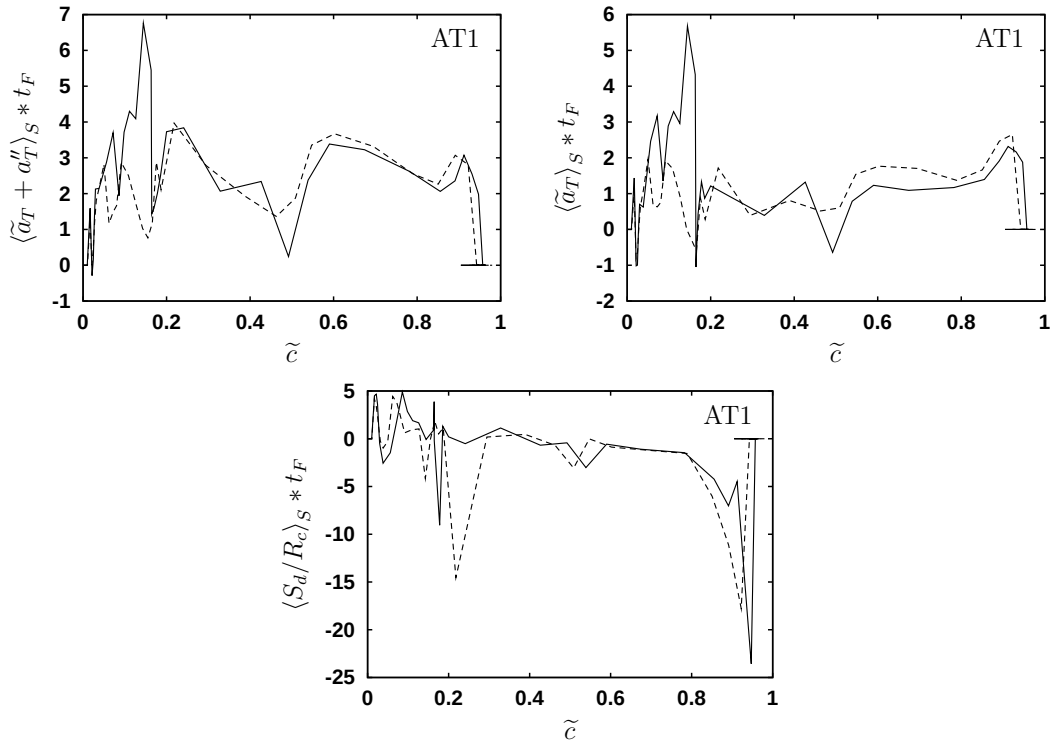

Figure 15. Flame surface mean value of total strain rate $\langle \widetilde{a}_T + a''_T \rangle_S$, mean flow induced strain rate $\langle \widetilde{a}_T \rangle_S$ and propagation term $\langle S_d/R_c \rangle_S$ as a function of the Favre averaged progress variable $\widetilde{c}$. Case AT1 with models M1 (solid line) and M2 (dashed line). All the quantities are normalized by the laminar flame time t_F.

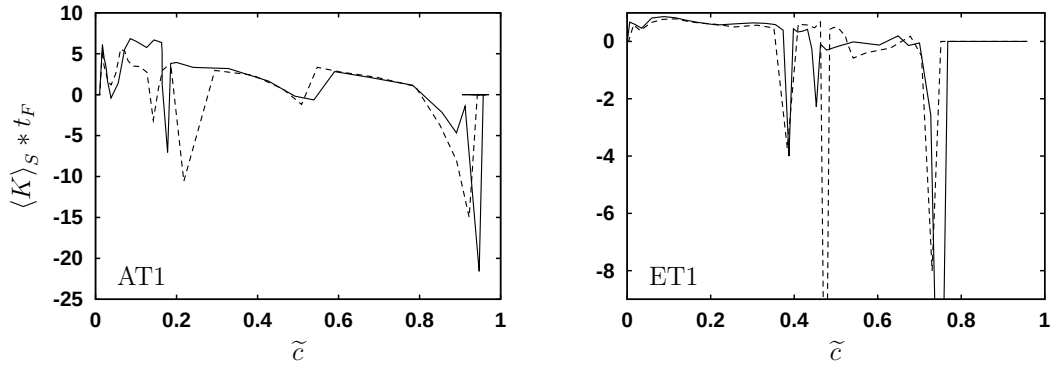

Figure 16. Flame surface mean value of the stretch $\langle K \rangle_S$ normalized by the laminar flame time t_F as a function of the Favre averaged progress variable $\widetilde{c}$. Cases AT1 and ET1 with models M1 (solid line) and M2 (dashed line).

Finally, we present in figure 16 the flame surface mean value of the stretch $\langle K \rangle_S$ as a function of the Favre averaged progress variable $\widetilde{c}$ for cases AT1 and ET1. In agreement with [6], the sign of the flame stretch is controlled by the propagation term, being positive in the fresh gases and negative in the burnt gases. Multicomponent transport has a significant impact on $\langle K \rangle_S$ in some regions of the turbulent flame. These regions are characterized by a highly wrinkled flame surface with large fluctuations of the propagation velocity. For example, in case ET1, the differences observed in figure 16 at $\widetilde{c} \approx 0.5$ are related to the flame front shown in figure 12 where the second from top pocket of fresh gases significantly differs between models M1 and M2.

7. Conclusions

In this paper we have performed for the first time DNS of various turbulent flames with detailed multicomponent transport models. Multicomponent transport models have been implemented using accurate and cost effective algorithms derived from recent theoretical results. The overall CPU time was only marginally increased when such algorithms were implemented in our DNS code. We have investigated fifteen turbulent premixed H_2/O_2 flames resulting from either flame/vortex or flame/turbulence interaction. Equivalence ratios ranged from 0.5 to 5. For flame/vortex interaction, we studied several flame behaviors, including formation of fresh gas pockets, vortex dissipation by strongly curved flames and flame quenching. For flame/turbulence interaction, we considered turbulent flames in both the standard and extended flamelet regimes.

For all configurations, multicomponent transport delays and enhances flame wrinkling, modifying global flame quantities such as flame surface area and integrated heat release. For most flames investigated here, this effect is not very pronounced and rarely exceeds a few percent in magnitude. It is however more important for lean and rich flames and in particular in the case of flame quenching. Moreover, multicomponent

transport has a significant impact on the propagation velocity in highly curved flames and therefore modifies flame stretch when curvature effects dominate strain.

Instantaneous snapshots of temperature and chemical species profiles confirm the influence of multicomponent transport in flames experiencing strong curvature. By modifying the concentration of active radicals and thus the propagation velocity, multicomponent transport leads locally to substantial changes in the geometrical features of the flame front. With an eye towards turbulent flame modeling, we also notice an impact of multicomponent transport on some of the source terms in the flame surface density equation. In the $\widetilde{c}$ space based on the Favre averaged progress variable, the magnitude of this impact is locally important. On the other hand, multicomponent transport may change global quantities such as flame brush or orientation factor by up to 7.5% for lean flames.

To sum up, detailed transport models may lead to large local modifications of turbulent flame properties (up to 50%). These changes are larger than those observed for laminar flames. However, turbulent fluctuations appear to filter out these effects when considering mean quantities, leading to much smaller changes (up to 7%). These results provide some a posteriori validation for most of the previous DNS based on simplified transport models. Nevertheless, considering our results, we may anticipate a very noticeable effect of transport models on the flame velocity in other configurations such as spherical flame kernels (small radius, curvature of constant sign preventing cancellation effects for mean values) placed in a weak turbulence field. We will be able to investigate this effect as soon as three-dimensional DNS becomes routinely feasible.

Acknowledgments

We acknowledge Professor D. Thévenin for fruitful discussions and N. Gourvitch for developing part of the postprocessing tools during his internship at Ecole Nationale des Ponts et Chaussées.

References

[1] Meneveau C and Poinsot T 1991 Stretching and quenching of flamelets in premixed turbulent combustion *Combust. Flame* **86** 311–332

[2] Veynante D, Trouvé A, Bray K N C, and Mantel T 1997 Gradient and counter-gradient scalar transport in turbulent premixed flames *J. Fluid Mech.* **332** 263–293

[3] Ashurst W, Kerstein A, Kerr R, and Gibson C 1987 Alignment of vorticity and scalar gradient with strain rate in simulated Navier-Stokes turbulence *Phys. Fluids* **30** 2343–2353

[4] Cattolica R J, Barr P, and Mansour N 1990 Propagation of a premixed flame in a divided-chamber combustor *Combust. Flame* **77** 101–121

[5] Poinsot T, Veynante T, and Candel S 1991 Quenching processes and premixed turbulent combustion diagrams *J. Fluid Mech.* **228** 561–606

[6] Trouvé A and Poinsot T 1994 The evolution of the flame surface density in turbulent premixed combustion *J. Fluid Mech.* **278** 1–31

[7] Baum M, Poinsot T, Haworth D C, and Darabiha N 1994 Direct numerical simulation of $H_2/O_2/N_2$ flames with complex chemistry in two-dimensional turbulent flows *J. Fluid Mech.* **281** 1–32

[8] Thévenin D, Behrendt F, Maas U, Przywara B, and Warnatz J 1996 Development of a parallel direct simulation code to investigate reactive flows *Comput. Fluids* **25**(5) 485–496
[9] Chen J Y and Im H G 2000 Stretch effects on the burning velocity of turbulent premixed hydrogen-air flames *Proc. Comb. Inst.* **28** In press
[10] Tanahashi M, Fujimura M, and Miyauchi T 2000 Coherent fine scale eddies in turbulent premixed flames *Proc. Combust. Inst.* **28** In press
[11] Ern A and Giovangigli V 1994 *Multicomponent Transport Algorithms* volume m 24 of *Lecture Notes in Physics*, New Series Monographs Springer-Verlag, Heidelberg
[12] Ern A and Giovangigli V 1995 Fast and accurate multicomponent transport property evaluation *J. Comput. Phys.* **120** 105–116
[13] Ern A and Giovangigli V 1996 The structure of transport linear systems in dilute isotropic gas mixtures *Phys. Rev. E* **53** 485–492
[14] Ern A and Giovangigli V 1996 Optimized transport algorithms for flame codes *Combust. Sci. Tech.* **118** 387–395
[15] Ern A and Giovangigli V 1998 Thermal diffusion effects in hydrogen-air and methane-air flames *Combust. Theory Model.* **2** 349–372
[16] Ern A and Giovangigli V 1999 Impact of detailed multicomponent transport on planar and counterflow hydrogen/air and methane/air flames *Combust. Sci. Tech.* **149** 157–181
[17] Cant R S, Rutland C, and Trouvé A 1990 A statistics for laminar flamelet modelling In *Proceedings of the Summer Program* pages 271–279 Center for Turbulence Research, Stanford University, USA
[18] Kuo K K 1986 *Principles of combustion* John Wiley and Sons
[19] Williams F A 1985 *Combustion Theory* Addison-Wesley (2nd edition)
[20] Giovangigli V 1999 *Multicomponent flow modeling* Birkhäuser, Boston
[21] Poinsot T and Veynante D 2001 *Theoretical and numerical combustion* Edwards, Philadelphia
[22] Volpe G 1991 On the use and accuracy of compressible flow codes at low Mach numbers *AIAA paper 91-1662*
[23] Majda A and Sethian J 1985 The derivation and numerical solution of the equations for zero Mach number combustion *Combust. Sci. Tech.* **42** 185–205
[24] Jackson T L, Macaraeg M G, and Hussaini M Y 1993 The role of acoustics in flame/vortex interactions *J. Fluid Mech.* **254** 579–603
[25] Prasad K 1994 Interaction of pressure perturbations with premixed flames *Combust. Flame* **97** 173–200
[26] Karlin V, Makhviladze G, and Roberts J 1998 Numerical algorithms for premixed flames in closed channels In Bruneau C.-H, editor, *Sixteenth International Conference on Numerical Methods in Fluid Dynamics*, Springer-Verlag, Heidelberg, 500–505
[27] de Charentenay J, Thévenin D, and Zamuner B 2001 Direct numerical simulations of turbulent H_2/O_2 premixed flames using compressible or low-Mach number formulations In *Direct and Large-Eddy Simulation IV* Twente, The Netherlands. Ercoftac Klüwer
[28] Miller J, Mitchell R, Smooke M, and Kee R J 1982 Toward a comprehensive chemical kinetic mechanism for the oxidation of acetylene : comparison of model predictions with results from flame and shock tube experiments *Proc. Combust. Inst.* **19** 181–196
[29] Waldmann L and Trübenbacher E 1962 Formale kinetische Theorie von Gasgemischen aus anregbaren Molekülen *Zeitschr. Naturforschg.* **17a** 363–376
[30] Ern A and Giovangigli V 1995 Thermal conduction and thermal diffusion in dilute polyatomic gas mixtures *Physica A* **214** 526–546
[31] Hirschfelder J O and Curtiss C F 1949 Flame propagation in explosive gas mixtures *Proc. Comb. Inst.* **3** 121–127
[32] Cook A W and Riley J J 1996 Direct numerical simulation of a turbulent reactive plume on a parallel computer *J. Comput. Phys.* **129** 263–283
[33] de Charentenay J, Thévenin D, and Zamuner B 2002 Comparison of direct numerical simulations

of turbulent flames using compressible or low-Mach number formulations *Int. J. Num. Methods in Fluids* Accepted for publication

[34] Kee R J, Rupley F M, and Miller J A 1989 Chemkin II : A Fortran chemical kinetics package for the analysis of gas phase chemical kinetics Technical Report SAND89-8009B Sandia National Laboratories

[35] Giovangigli V and Darabiha N 1988 Vector computers and complex chemistry combustion In *Proc. Conference Mathematical Modeling in Combustion and Related Topics* volume 140 pages 491–503. NATO Adv. Sci. Inst. Ser. E, Brauner C and Schmidt-Lainé C (Eds.)

[36] Ern A and Giovangigli V 1996 [http://www.cmap.polytechnique.fr/www.eglib], Eglib server with user's manual

[37] Kee R J, Dixon-Lewis G, Warnatz J, Coltrin M E, and Miller J A 1986 A Fortran computer code package for the evaluation of gas-phase multicomponent transport properties Technical Report SAND86-8246 Sandia National Laboratories

[38] Giovangigli V and Smooke M D 1987 Extinction of strained premixed laminar flames with complex chemistry *Combust. Sci. Tech.* **53** 23–49

[39] Giovangigli V and Smooke M D 1989 Adaptive continuation algorithms with application to combustion problems *Appl. Numer. Math.* **5** 305–331

[40] Candel S M and Poinsot T J 1990 Flame stretch and the balance equation for the flame area *Combust. Sci. Tech.* **70** 1–15

[41] Pope S B 1988 Evolution of surfaces in turbulence *Int. J. Eng. Sci.* **26** 445–469

[42] Renard P H, Rolon J C, Thévenin D, and Candel S 1999 Investigations of heat release, extinction and time evolution of the flame surface for a non-premixed flame interacting with a vortex *Combust. Flame* **117** 189–205

[43] Hasegawa T, Morooka T, and Nishiki S 2000 Mechanism of interaction between a vortex pair and a premixed flame *Combust. Sci. Tech.* **150** 115–142

[44] Renard P H, Thévenin D, Rolon C, and Candel S 2000 Dynamics of flame/vortex interactions *Prog. Energy Combust. Sci.* **26**(3) 225–282

[45] Hinze J O 1975 *Turbulence* McGraw Hill Book Company (2nd edition)

[46] Bray K N C 1990 Studies of the turbulent burning velocity *Proc. R. Soc. Lond. A* **431** 315–335